ACS NANO
Cite This: ACS Nano 2018, 12, 4512−4520
www.acsnano.org

ARTICLE

Inverse Stellation of CuAu-ZnO Multimetallic-Semiconductor Nanostartube for Plasmon-Enhanced Photocatalysis

Chuan Fu Tan,[†,‡] Aung Kyi Su Su Zin,[†] Zhihui Chen,[§] Chi Hao Liow,[†] Huy Thong Phan,[∥] Hui Ru Tan,[⊥] Qing-Hua Xu,[§] and Ghim Wei Ho*[,†,∥,⊥]

[†]Department of Electrical and Computer Engineering, National University of Singapore, 4 Engineering Drive 3, Singapore 117583
[‡]NUS Graduate School for Integrative Sciences and Engineering, National University of Singapore, Centre for Life Sciences, #05-01, 28 Medical Drive, Singapore 117456
[§]Department of Chemistry, National University of Singapore, 3 Science Drive 3, Singapore 117543
[∥]Engineering Science Programme, National University of Singapore, 9 Engineering Drive 1, Singapore 117575
[⊥]Institute of Materials Research and Engineering, A*STAR (Agency for Science, Technology and Research), 3 Research Link, Singapore 117602

Supporting Information

ABSTRACT: One-dimensional (1D) metallic nanocrystals constitute an important class of plasmonic materials for localization of light into subwavelength dimensions. Coupled with their intrinsic conductive properties and extended optical paths for light absorption, metallic nanowires are prevalent in light-harnessing applications. However, the transverse surface plasmon resonance (SPR) mode of traditional multiply twinned nanowires often suffers from weaker electric field enhancement due to its low degree of morphological curvature in comparison to other complex anisotropic nanocrystals. Herein, simultaneous anisotropic stellation and excavation of multiply twinned nanowires are demonstrated through a site-selective galvanic reaction for a pronounced manipulation of light−matter interaction. The introduction of longitudinal extrusions and cavitation along the nanowires leads to a significant enhancement in plasmon field with reduced quenching of localized surface plasmon resonance (LSPR). The as-synthesized multimetallic nanostartubes serve as a panchromatic plasmonic framework for incorporation of photocatalytic materials for plasmon-assisted solar fuel production.

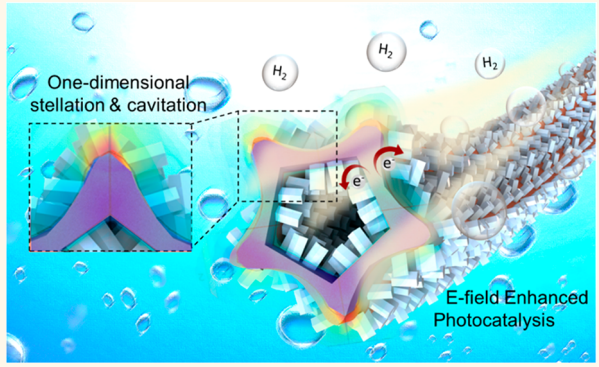

KEYWORDS: *metal−semiconductor, CuAu-ZnO, nanotube, plasmonic, photocatalysis*

Surface plasmons (SPs), generated from the interactions of photons and material interfaces, are extensively exploited in nanophotonic devices,[1] biological sensors,[2,3] medical therapies,[4,5] optical spectroscopy,[6,7] and solar-harnessing systems.[8−10] Since the advent of nanoscience, various nanomaterials with elevated surface plasmon resonances have been engineered to accommodate these diverse and growing assortments of plasmon-related research.[11−14] Of all these emerging fields, plasmonic photocatalysis is perceived as a promising sustainable technology which benefits from a higher charge-separation efficiency and photosensitivity in the visible and near-IR region.[15−18] Specifically, 1D metallic nanomaterials are deemed to be excellent candidates for photocatalysis due to their high surface reaction sites to support photocatalytic materials and exceptional conducting medium for efficient charge transport and separation.[19−22] However, developing LSPR-enhanced absorption in 1D materials has proven to be nontrivial, due to the seemingly unalterable crystal growth habits and morphological architectures of face-centered cubic (fcc) nanowires. Often, modifications involving complex and multiple steps are needed to improve LSPR characteristics, such as hybridization with other nanostructures.[23−25]

Herein, a one-pot approach toward stellated Cu and Au bimetallic alloy nanotubes is demonstrated on the basis of site-specific galvanic reactions. The synthesis is mediated by longitudinal crystal defects and facet passivation that facilitate

Received: January 30, 2018
Accepted: April 26, 2018
Published: April 26, 2018

DOI: 10.1021/acsnano.8b00770
ACS Nano 2018, 12, 4512−4520

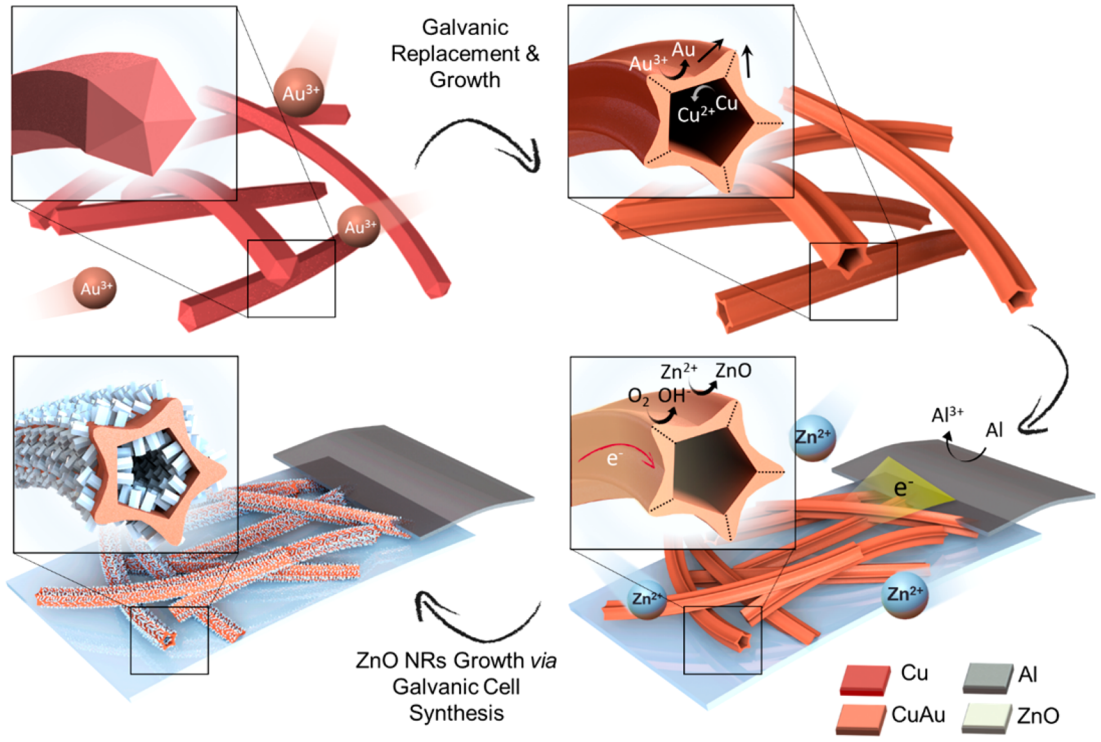

Figure 1. Schematics of twinned planes-directed galvanic replacement in the formation of CuAu nanostartubes from Cu nanowires. The subsequent growth of ZnO NRs on CuAu nanostartubes was conducted *via* electroless galvanic cell synthesis.

simultaneous hollowing and stellation of multiply twinned pentagonal Cu nanowires. The creation of sharp longitudinal vertices of the resultant nanostartubes (NSTs) assists in confining background electromagnetic oscillations to enhance the efficiency of plasmon-assisted light harvesting. Moreover, the as-synthesized CuAu bimetallic NSTs not only exploit the inexpensive nature of Cu and high stability of Au but also utilize the hybridized SPRs of Cu and Au to achieve a broadband solar absorption. To assess its panchromatic absorption characteristics, catalytically active yet plasmonic impoverished ZnO nanorods (NRs) are judiciously grown on the NSTs for evaluation of plasmon-enhanced photocatalysis. In this configuration, the establishment of plasmonic metal−semiconductor heterojunctions maximizes the charge separation of hot electrons and improves the light-harvesting capabilities without a tradeoff between the individual CuAu NST and ZnO NR properties. This is unlike the case for the latter material, which has traditionally been limited by narrow ultraviolet absorption range and high charge recombination drawbacks. Accordingly, an exceptional broad-band photoreactivity is realized by the augmented hierarchical multimetallic-semiconductor plasmonic nanohybrids with efficient charge transfer and plasmon-induced charge generation attributes.

RESULTS AND DISCUSSION

Figure 1 illustrates the general synthesis pathway of the CuAu NST-ZnO nanostructures. As reported previously,[26] a Maillard reaction was employed in the synthesis of Cu NWs, for which the precursors consist of nontoxic amino acids, amines, and glucose. After 3 h into the synthesis, gold chloride solutions with varying amounts of hexadecylamine (HDA) were injected to quench the growth of Cu NWs and initiate the site-selective galvanic replacement process. On the basis of the higher reduction redox potential of Au ions relative to that of Cu, replacement of Cu to Au will occur, with a distinct change in color from bright red to dark brown (Figure S1a).[27] This *in situ* addition of Au^{3+} ions during the growth of Cu NWs is necessary to ensure that the oxidation of Cu is kept to a minimum with a reaction environment of reducing agent. The reaction mixture was then allowed to proceed for the completion of the replacement process and subsequently quenched in an ice bath. Excess surfactants and precursors were then removed *via* centrifugation, and a high yield of CuAu NSTs was obtained, as seen under a scanning electron microscope (SEM) in Figure S1b. The evolution of nanowires with a pentagonal cross section to a nanotube with a star-shaped cross section is shown in SEM images in Figure S2, where the morphological dissimilarities are clearly observed in both longitudinal and transverse directions of the nanostructures.

A galvanic cell synthesis approach that was presented in our previous works is employed to incorporate ZnO NRs to the as-synthesized CuAu NST.[19,28] The electroless deposition technique does not need any current or voltage source, since electrons are generated from spontaneous redox reactions. Al foil is used as an inexpensive sacrificial electron source to deliver electrons to the cathode for selective oxidative growth of ZnO NRs on any conductive substrate. The reaction begins with the generation of OH^- ions from the thermal decomposition of hexamethylenetetramine to ammonia. As the galvanic cell reaction progresses, aluminum oxidizes to form $Al(OH)_3$ and releases electrons in the process. The electrons are conducted through the interconnected network of CuAu NSTs which direct the reduction of Zn^{2+} ions on the surface of NSTs. The exceptional conductivity of the NSTs (Figure S3) enables them to serve as one-dimensional nanocathodes in this galvanic cell process, illustrated in Figure S4. The uniform charge transfer and distribution allow a conformal growth of

DOI: 10.1021/acsnano.8b00770
ACS Nano 2018, 12, 4512−4520

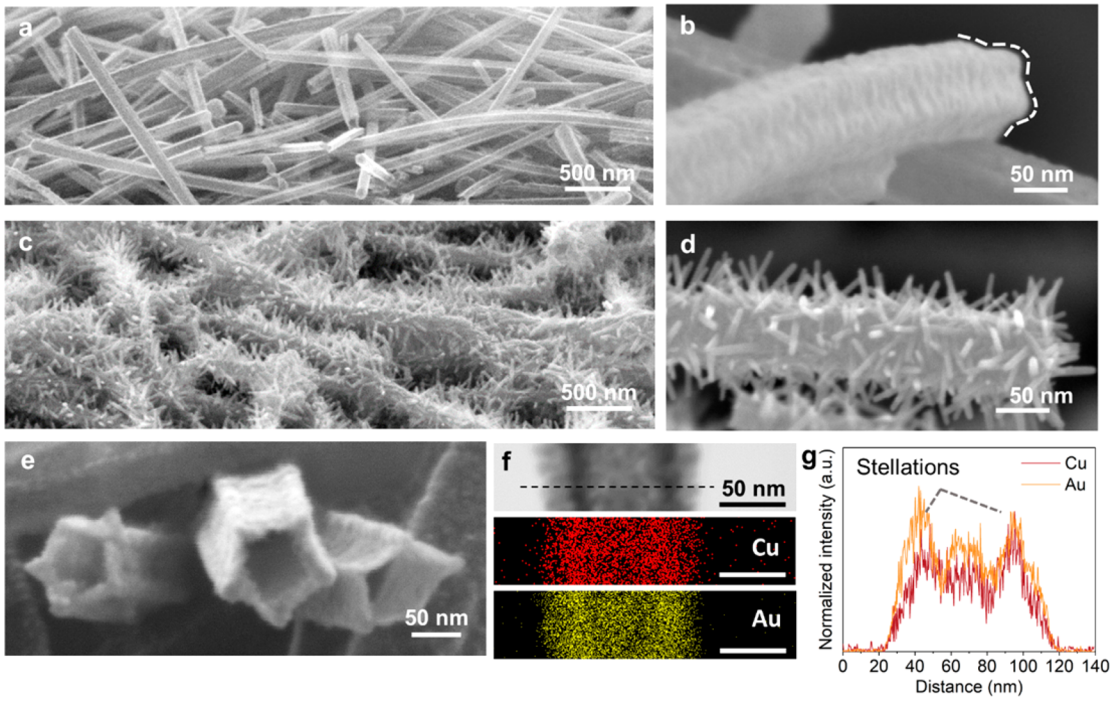

Figure 2. SEM images of (a, b) CuAu NSTs and (c, d) CuAu NST-ZnO. (e) Cross-sectional view of CuAu NSTs. (f) TEM-EDX mapping and (g) line spectra of CuAu NSTs.

ZnO NRs on the 1D NST surface without the need for a ZnO seed layer on the CuAu NST prior to the growth. A time study of the growth evolutions of ZnO NRs on CuAu NSTs over 30, 60, and 180 min durations is shown in Figure S5.

SEM images of CuAu NSTs and CuAu NST-ZnO are shown in Figure 2a–d. Nanogrooves, outlining the starlike profile, can be clearly observed along the longitudinal direction of the NST in Figure 2b, suggesting that the star-shaped cross section spans the entire length of the nanostructure. The growth of the ZnO NRs on the NSTs is shown in Figure 2d. The cross-sectional morphologies of the CuAu NSTs are depicted in Figure 2e and Figure S6. By extrapolating a line from each of the vertices of the star to the center of the nanowire (Figure S6d), it can be concluded that the inverse stellations originated from the twinning planes along the remnant Cu NW pentagonal core. In order to estimate the composition of CuAu NST, energy-dispersive X-ray spectroscopy (EDX) was conducted on the CuAu NST (Figure 2f), which estimated the Cu:Au atomic ratio to be approximately 0.47:0.53. An even distribution of Cu and Au is observed across the length of the transverse section of the NST (Figure 2g). The chemical compositions of the Cu NWs, CuAu NSTs, and CuAu NST-ZnO are presented in the SEM-EDX spectra of Figure S7.

The proposed mechanism for the formation of the hollow star-shaped cross section is illustrated in Figure 3a and Figure S8. The growth of Cu NWs begins with a 5-fold multiply twinned seed crystal.[29] In the presence of HDA, further growth is confined in the Cu [110] direction by the passivation of the {100} facets. Upon the introduction of Au ions, a difference in redox potentials drives the oxidation of Cu and reduction of Au^{3+} ions. In line with other galvanic replacement reaction reports,[27,30,31] the formation begins with an alloyed CuAu shell on the exterior surface of the Cu NWs. A significant amount of Au is seen deposited on the edges of the Cu NWs (Figure S9a,b). Subsequently, growth of the shell thickness with concurrent out-diffusion of Cu ensues, facilitated by further redox reactions between Cu and Au^{3+} ions and the reducing environment.[27] The can be seen with the reduction in mass contrast of the Cu core and concurrent thickening of the pentagonal edges in the TEM images of Figure S9c,d. The final morphology is a nanotube structure with spatially overlapped Cu and Au content within the stellated shell, as seen in the EDX mapping and line spectrum of Figure S9e,f. The synthesis procedure and structure of the CuAu NSTs differ from the conventional 1D pentagonal design.[30,32,33] It is postulated that the difference stems from the procedural alteration in which the galvanic replacement takes place in the same environment as the growth of the nanowires. This allows the reaction to occur in the presence of facet passivating agents that are compliant to both Cu and Au, whereas in other works, NWs are usually extracted and removed from any residual surfactant prior to the replacement process.[34−36] The unperturbed, direct sequential process in this work is believed to preserve the crystallinity and purity of the nanowires, while ensuring minimum disturbance to the facet capping ligands.

After investigation of the influence of various reagents in the replacement process, it is found that HDA plays a pivotal role in facilitating the starlike protrusions of the nanotube. As illustrated in the reaction pathways of Figure 3a, when additional HDA is used in the galvanic replacement, a shorter extent of stellations of the nanostartubes (CuAu sNSTs) is observed. Moreover, pentagonal nanotubes (CuAu NTs) are formed when an excess amount of HDA is added with the Au salt solution. The SEM images of the differing cross-section geometries of the nanotubes are shown in Figure 3b–d. Assuming the same core structure, the extent of anisotropic protrusions can be estimated by comparing the effective diameters of the NSTs, tabulated in Figure 3e. With an increased addition of HDA, the effective diameter of the NST is reduced, which is in agreement with the decrease in the length

DOI: 10.1021/acsnano.8b00770
ACS Nano 2018, 12, 4512−4520

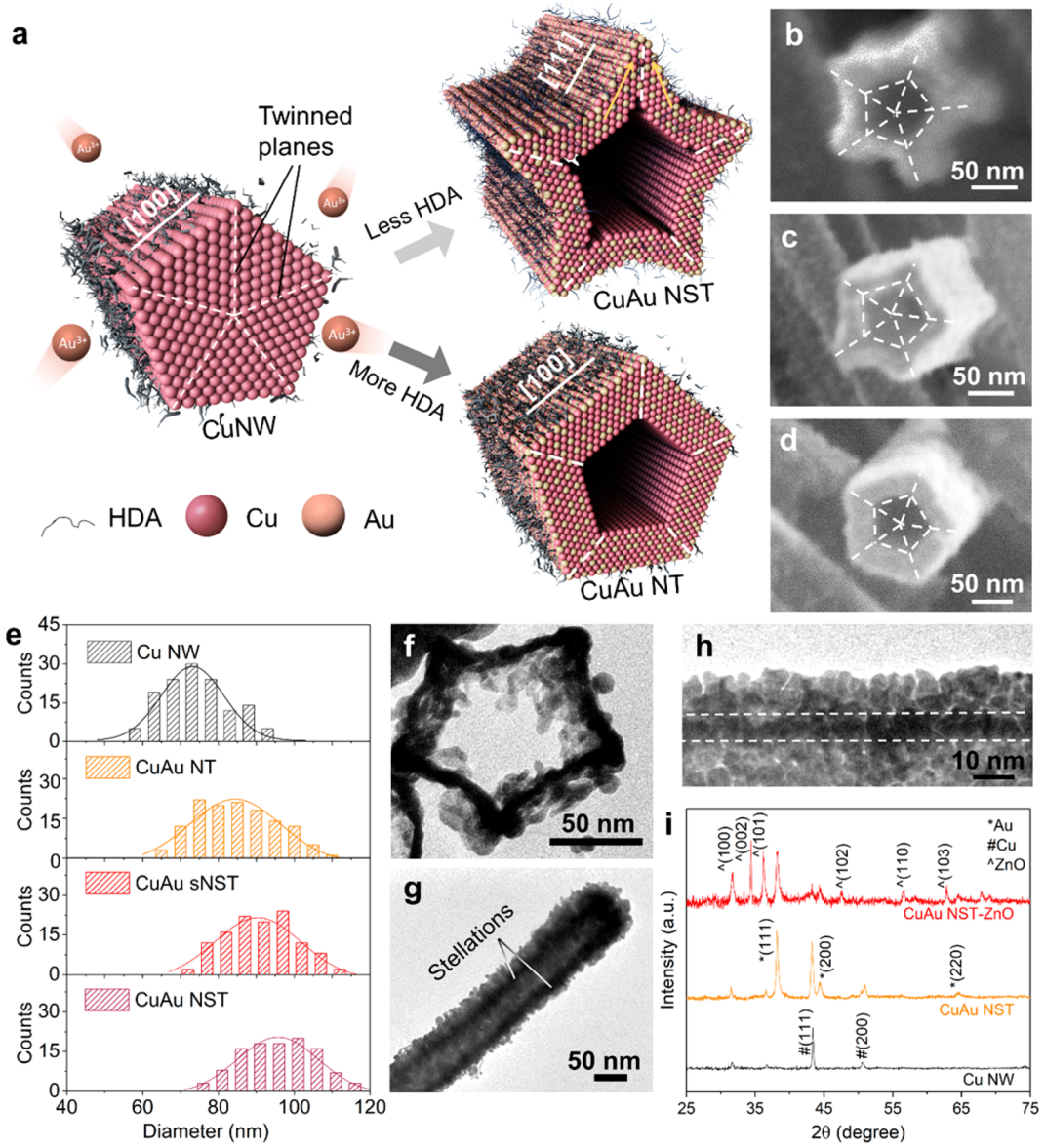

Figure 3. (a) Schematic illustration of modulating stellations of CuAu NST with varied amounts of HDA. SEM images of (b) NST, (c) sNST, and (d) NT. (e) Diameter distribution of Cu NWs, CuAu NTs and NSTs. (f) Cross-sectional and (g, h) top view TEM images of the CuAu NST with marked stellated regions. (i) XRD spectra of Cu NWs, CuAu NSTs, and CuAu NST-ZnO.

of stellations as seen in Figure 3c,d. In the formation of particle-based nanostars, He *et al.* and Bazán-Díaz *et al.* reported that HDA assists in the star-shaped creation by preferential passivation of the {111} and {100} facets. This increases the inclination of growth along the twinned planes.[37,38] It is believed that the same conclusion can be made with a one-dimensional nanomaterial of similar composition, as seen in our work. Interestingly, the presence of an elevated amount of HDA leads to excessive passivation on both facets, which consequently results in a more isotropic growth. However, in an environment with a minimum amount of HDA, passivation of the {111} facet is more prominent. This consequently provides a means of modulating the extent of stellations from the nanotube. It is noted that, by changing the amount of HDA in the initial growth solution, the shape of the resulting Cu nanocrystals can change drastically. Subsequent galvanic replacement results in formation of hollow polygons such as nanoboxes and nanorods, as seen in Figure S10. Cross-sectional TEM and SEM images of the NSTs obtained by ultramicrotomy are shown in Figure 3f and Figure S11, revealing defined stellations across a large quantity of NSTs. TEM images of the surface of the NSTs are shown in Figure 3g,h. The crystal structure of the CuAu NST has also been investigated with X-ray powder diffraction (XRD). The respective XRD spectra in Figure 3i depict Cu (111) and (200) diffraction peaks at 43.5 and 50.7°, respectively. Additional diffraction peaks of the CuAu NST are found at 38.2 and 44.6°, which are indexed to Au (111) and (200) facets, respectively. The chemical composition of CuAu NSTs has been further analyzed with X-ray photoelectron spectroscopy (XPS) (Figures S12 and S13). An increased stability toward oxidation is observed with CuAu NSTs, as the amalgamation with Au increases the overall oxidative resistance of the bimetallic CuAu NSTs. On comparison of the Cu XPS spectra of Cu NWs and CuAu NSTs, a more significant Cu^{2+} peak, attributed to oxidation, is observed for the pure Cu NWs (Figure S14).

DOI: 10.1021/acsnano.8b00770
ACS Nano 2018, 12, 4512−4520

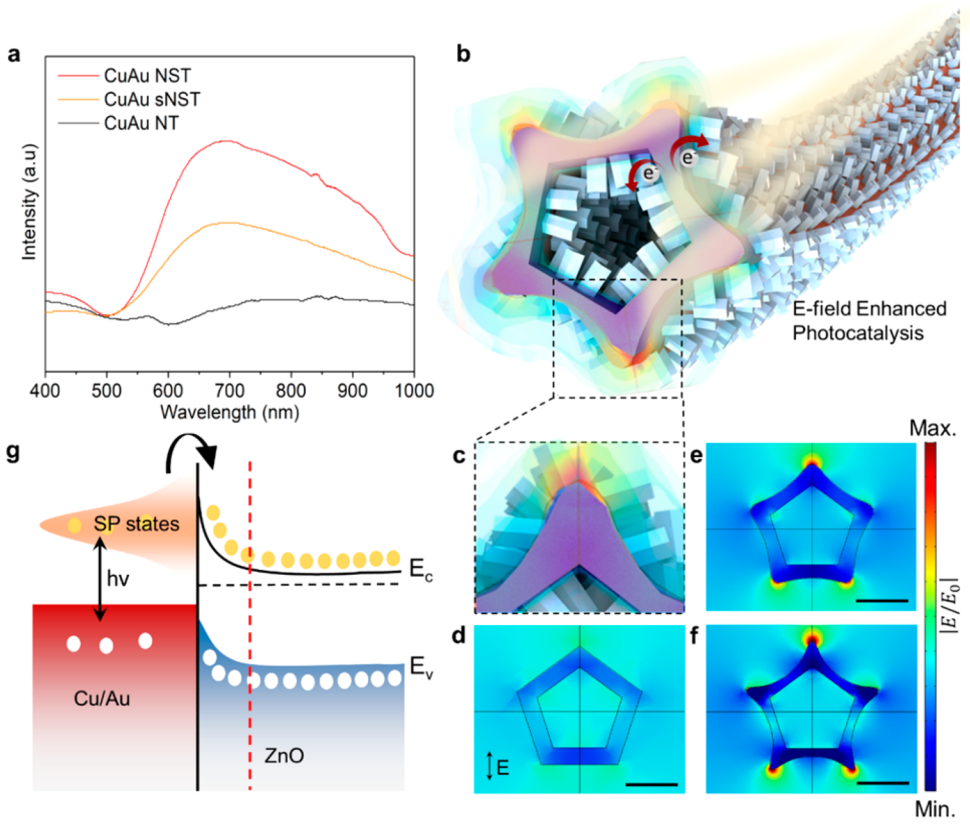

Figure 4. (a) UV−vis extinction spectrum of CuAu NTs, CuAu sNSTs, and CuAu NSTs. (b, c) Schematic illustration of E-field enhanced photocatalysis of CuAu NST-ZnO. FEM simulations of E-field distribution of (d) CuAu NTs, (e) CuAu sNSTs, and (f) CuAu NSTs at 700 nm. (g) Band diagram of hot electron injection from CuAu NST to ZnO. The scale bar is 40 nm.

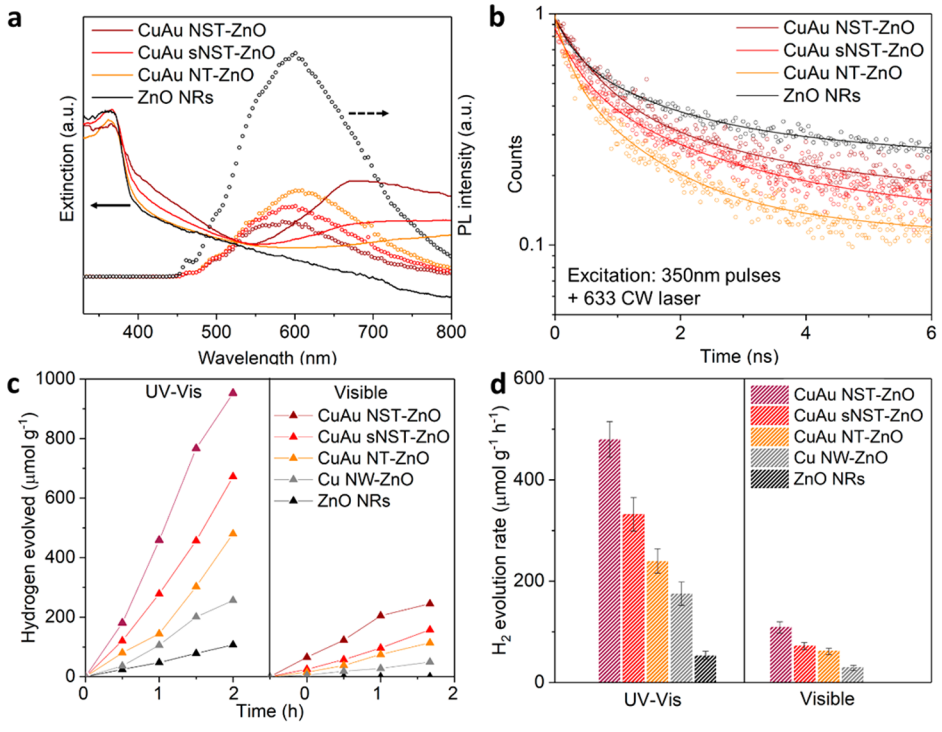

Figure 5. (a) UV−vis extinction and photoluminescence spectra and (b) CW-assisted time-resolved photoluminescence of ZnO and CuAu NT-ZnO, sNST-ZnO, and NST-ZnO. (c) Hydrogen generation under UV−vis and visible illumination. (d) Hydrogen generation rates of ZnO NRs, Cu NWs, CuAu NT-ZnO, CuAu sNST-ZnO, and CuAu NST-ZnO.

DOI: 10.1021/acsnano.8b00770
ACS Nano 2018, 12, 4512−4520

To investigate the plasmon-enhanced characteristics of the stellated NST-ZnO composite, a finite-difference time-domain (FDTD) method was employed to examine the wavelength-dependent photoabsorption of the CuAu nanostructures. To simplify the optical parameters, the dielectric constant of CuAu composition is approximated with an average composition weightage of Cu and Au from prior EDX analysis (Figure S15).[39] Broad extinction spectra from the visible to the near-IR region of 500−1000 nm for the stellated nanostructures are obtained and are shown in Figure S15. This is in agreement with experimental measurements of Figure 4a, which suggests a broad-band photosensitivity of the materials. In addition, finite element method (FEM) simulations were used to study the local electric fields response of NSTs, sNSTs, and NTs under external light excitation. The electric fields of NSTs, sNSTs, and NTs were simulated around the plasmon extinction peak at 700 nm, and as expected, a much higher local electric field is observed at the vertices of the nanostructures, as illustrated in Figure 4b−f. From the simulations, the relative magnitudes of the E-field enhancement at the tips of sNSTs and NSTs to that of NTs are 5.9 and 3.5, respectively. The increasing intensities of the local E-fields from NSTs and sNSTs to NTs are ascribed to the higher degree of morphological curvatures of the nanostructures. The local E-field amplification can be correlated to several processes for plasmon-enhanced photocatalysis: near-field enhancement, scattering, Förster resonance energy transfer (FRET), and plasmon-induced resonant energy transfer (PIRET).[8,16,40] The enhanced electromagnetic near field of the excited plasmonic CuAu nanostructure heightens the electron−hole pair formation in the ZnO NRs, which is in close proximity to the tip of the stellations. Due to the relatively large dimensions of the CuAu NTs, sNSTs, and NSTs, scattering effect is postulated to be significant, which improves light utilization by increasing the average path length of photons in the composites. Since ZnO is a large band gap semiconductor, spectral overlap between the absorption spectra of the semiconductor and the plasmon resonance band of CuAu structures is limited. This suggests that the effects of PIRET or FRET processes are minimum.[40] Other than the contributions from an elevated local E-field, direct electron transfer, in a form of hot electron injection, is another critical process in plasmon-enhanced photocatalysis. Taking into account the band alignment of CuAu and ZnO, the mechanism of hot electron transfer from the enhanced local electric field is illustrated in the schematic of Figure 4g.[41] Upon excitation of the SPs of CuAu NST, hot electrons with energy higher than the Schottky barrier can be injected into the conduction band of ZnO to increase the amount of photoinduced charge carriers for photocatalysis.[42,43]

The understanding of how photons interact with the multimetallic-semiconductor nanohybrids can be inferred from the extinction and photoluminescence (PL) of the ZnO-composite materials in Figure 5a. The extinction spectral band centered at 360 nm corresponds to the band gap of ZnO, whereas the band starting from 540 nm relates to the plasmon band of CuAu NST. A slight red shift in the plasmon band is noted, presumably due to the higher dielectric coefficient environment of ZnO.[44] The characteristic trend of having a higher visible extinction with more pronounced stellations coincides with the earlier optical results of CuAu NTs and NSTs presented in Figure 4. Photoluminescence was conducted under excitation at 350 nm, and a stark decrease in the defect band emission of ZnO, centered at 600 nm, is observed with samples that are composited with CuAu NTs and NSTs. This can be attributed to the reduced charge recombination with the existence of viable charge transfer pathways to the CuAu core. The visible emission intensity is observed to further decline with an increased in the stellation length. This can be associated with the SP-mediated absorption by the bimetallic core, as the plasmon band of CuAu NST overlaps with the defect emission band of ZnO.[45,46] Consequently, the quenching of visible emission through energy transfer to excite the SPs of the NSTs takes place.

Picosecond-resolved fluorescence decay analysis was conducted to further investigate the emission and charge recombination dynamics of the as-synthesized samples. A continuous wave-assisted time-resolved PL (CW-assisted TRPL) spectroscopic configuration, developed by Chiu et al., was employed to reveal the role of plasmon-related charge transfer.[47] This method involves a simultaneous femtosecond pulsed UV irradiation and continuous wave illumination at the band gap and plasmon peak, respectively. The measured and fitted results of the CW assisted-TRPL are shown in Figure 5b and Figure S16 and Table S1. Under 350 nm pulsed excitation without CW illumination, average exciton lifetimes of 33.27, 8.32, 10.37, and 11.00 ns are obtained for ZnO NRs, CuAu NT-ZnO, CuAu sNST-ZnO, and CuAu NST-ZnO, respectively. It can be seen that through charge transfer with the presence of the metallic CuAu core, the lifetimes of the excited states of the composites are much shorter than that of the pure ZnO. To further inspect the influence of SPR excitation on the excited states of the composites, a CW irradiation of 633 nm wavelength was used concurrently with the pulsed 350 nm excitation. Upon this secondary irradiation, which is closer to the plasmon-absorption band, the average lifetimes obtained for ZnO NRs, CuAu NT-ZnO, CuAu sNST-ZnO, and CuAu NST-ZnO evolved to 33.55, 11.31, 15.74, and 18.62 ns, respectively. It can be seen that the exciton lifetimes of CuAu-ZnO composites increased while that of ZnO remained relatively invariant. The extended lifetimes are postulated to indicate the establishment of a charge transfer pathway that is facilitated by plasmon excitation. Moreover, photogenerated charge carriers of ZnO can be vastly enhanced by hot electron injection and intense local electric fields of the CuAu SPRs, which would further contribute to a delay in the decay of the excited states. The band diagram for the CW-assisted TRPL spectroscopic configuration is illustrated in Figure S16a, denoting the simultaneous excitation of CuAu plasmon and ZnO states. Considering the different charge relaxation and generation pathways, the rate of excited state decay (S*) can be expressed as

$$\frac{d[S^*]}{dx} = (-k_{rec} - k_{ct} + k_{SPR})[S^*] \quad (1)$$

where k_{rec}, k_{ct}, and k_{SPR} correspond to the rate constants of radiative charge recombination, nonradiative charge recombination, and carrier generation by SPR.[47] The increment of lifetimes by approximately 35.9, 51.8, and 69.3% of CuAu NT-ZnO, CuAu sNST-ZnO, and CuAu NST-ZnO upon simultaneous 633 nm irradiation suggests that the enhancement in carrier generation by SPR has a positive relation to the extent of stellations. This can be attributed to local electric field amplification, as discussed in Figure 4.

Finally, the hierarchical plasmonic nanohybrids are evaluated as photocatalysts for hydrogen generation to investigate their plasmon-assisted light harnessing performance. Figure 5c shows

DOI: 10.1021/acsnano.8b00770
ACS Nano 2018, 12, 4512−4520

the hydrogen evolution under UV and UV−vis radiation where ZnO (Figure S17a,b), Cu NW-ZnO (Figure S17c,d), CuAu NT-ZnO, sNST-ZnO, and NST-ZnO were tested. Cu NW-ZnO was synthesized using similar procedures and used as a controlled sample. It can be observed that the CuAu NST-ZnO attains the highest hydrogen production rate under both UV−vis and visible irradiation. Without any plasmon-assisted absorption or scattering, ZnO NRs do not yield a measurable amount of H_2 under visible light illumination. Meanwhile, Cu NW-ZnO exhibits a comparatively lower hydrogen generation rate in comparison to that of the CuAu analogues. This may be accounted for by a lower light extinction of the unstellated structures, a decrease in surface reaction sites with a solid core and the absence of Au SPs that broaden the absorption energy range. For the CuAu plasmonic nanohybrid, higher hydrogen production is validated for both the UV−vis and visible regions, as plotted in Figure 5d. Notably, CuAu NST-ZnO has a hydrogen production rate of 480 μmol/g, which is ∼9 times higher than that of pure ZnO. A much lower increment is observed when a physical mixture of CuAu NST and ZnO NRs is tested (Figure S18). This shows the importance of establishing a direct and intimate interface between the metal and semiconductor to facilitate efficient charge transfer. The vastly improved photocatalytic performance can be correlated to the synergistic combination of plasmon enhanced field intensity, higher broad-band absorption, and reduced charge recombination.

CONCLUSIONS

In summary, we have demonstrated the synthesis of one-dimensional metallic crystals which take an unusual form of stellated and hollow bimetallic-semiconductor nanostartubes with panchromatic light absorption ability. A pronounced plasmonic field enhancement is enabled by the simultaneous cavitation and acute extensions of multiply twinned nanowires. With an elevated magnitude of SPRs excited across a broad range of wavelengths, a significant improvement in plasmon-mediated photocatalytic hydrogen generation has been achieved. The understanding of facet-specific galvanic replacement, compliant to a multimetallic nanomaterials system, greatly facilitates the morphological alterations to directly influence the plasmonic properties. This supports the development of highly efficient panchromatic plasmonic nanomaterials for various functional solar energy conversion applications.

EXPERIMENTAL SECTION

Synthesis of Cu NWs. The synthesis of Cu NWs was reported in a previous work.[26] Briefly, 0.03 g of anhydrous copper chloride ($CuCl_2$, Sigma-Aldrich), 0.18 g of 1-hexadecylamine (HDA, Sigma-Aldrich), and 0.5 g of polyvinylpyrrolidone (PVP average mol wt 10000, Tokyo Chemical Industry) were added to 10 mL of deionized (DI) water. The mixture was then stirred vigorously overnight. A 0.6 g portion of glucose ($C_6H_{12}O_6$, Sigma-Aldrich) was subsequently added into the growth solution, and immediately thereafter, it was sealed and placed into an oil bath at 100 °C with stirring for 3 h.

Synthesis of Copper−Gold Nanostartubes (CuAu NSTs). After Cu NWs were formed, 0.5 mL of a 0.085 M Au salt solution ($HAuCl_4$) was added to the reaction mixture at rate of 0.1 mL/min. For mild suppression of stellations to form short-stellated NSTs (sNSTs), 0.25 M HDA was added together with the Au salt solution while 0.5 M HDA was added for a total suppression of the stellations to form CuAu nanotubes (NTs). The reaction was allowed to continue at 100 °C for 1 h to ensure it was complete. The NSTs were obtained *via* centrifugation at 4000 rpm for 5 min. Solvent exchange was conducted with ethanol followed by hexane to remove byproducts and excess ligands.

Synthesis of CuAu NSTs Modified with Zinc Oxide Nanorods (CuAu NST-ZnO). Zinc oxide NRs (ZnO NRs) were grown on the NST by a galvanic cell reaction. First, the growth solution was prepared with equimolar (25 mM) zinc nitrate ($Zn(NO_3)_2$) and hexamethylenetetramine (HMT) in 50 mL of deionized water. CuAu NSTs were vacuum-filtered onto a PTFE filter membrane, which was then prepared for the deposition process. The filter membranes containing the NSTs were mounted onto a glass plate with aluminum foil secured at both ends with Teflon tape. The prepared samples were then submerged in the prepared growth solution and placed in the oven at 80 °C for 3 h.

Photocatalytic Measurements. A 10 mg portion of the photocatalyst was dispersed in 10 mL of a 9/1 water/methanol mixture in a 25 mL sealed quartz cylindrical reaction cell. The cell was illuminated with a 300 W xenon arc lamp of intensity 100 mW cm^{-2}. The H_2 gas produced was extracted periodically from the photocatalytic experiments and measured by gas chromatography (Shimadzu GC2010 TCD). Experiments involving visible light irradiation were carried out using a 420 nm cutoff filter.

Materials Characterization. The morphologies of the heterostructures were characterized with a scanning electron microscope (SEM, JEOL FEG JSM 7001F) operated at 15 kV and a transmission electron microscope (JEOL 2100 TEM). The elements present in the nanostructures were analyzed using energy dispersive X-ray (EDX, Oxford Instruments). The crystalline structures and elemental compositions of the materials were analyzed using XRD (D5005 Bruker X-ray diffractometer equipped with graphite-monochromated Cu Kα radiation at λ = 1.541 Å). Extinction spectra of the samples were measured with an UV−vis−NIR spectrophotometer (UV−vis, Shimadzu UV-3600). Continuous-wave-assisted time-resolved photoluminescence measurements were performed under excitation of 350 nm femtosecond pulses and a 633 nm CW laser. The UV excitation source used was a mode-locked Ti:sapphire laser (Chameleon Ultra II, Coherent) working at a repetition rate of 80 MHz and a pulse duration of 140 fs. The second-harmonic generation of 700 nm output from the laser was employed to excite the samples. The pulse energy of the femtosecond laser was 120 pJ per pulse. The excitation laser pulses were focused onto the sample through an objective (×10, NA = 0.3) with a spot size of ∼0.7 μm. The energy density at the excitation spot was 6.5 mJ cm^{-2}. The scattering of the excitation laser pulses was suppressed by using a 412 nm long-pass filter. The power density of the CW laser used was 52 mW cm^{-2}, and the scattering was suppressed with a 600 nm short-pass filter. The photoluminescence was detected and collected by a photon-counting photomultiplier (PMA, Picoquant). The emission centered at 590 nm was selected by a monochromator (SpectroPro 2300i, Princeton Instrument). The PL decay dynamics were achieved by a time-correlated single photon counting module (TCSPC Picoharp300, Picoquant).

ASSOCIATED CONTENT

Supporting Information

The Supporting Information is available free of charge on the ACS Publications website at DOI: 10.1021/acsnano.8b00770.

Additional schematics, SEM and TEM images, conductivity, EDX, and XPS measurements, calculation of optical parameters and photoluminence lifetime of CuAu composites, and hydrogen generation of a physical mixture of CuAu NST and ZnO NRs (PDF)

AUTHOR INFORMATION

Corresponding Author

*E-mail for G.W.H.: elehgw@nus.edu.sg.

ORCID

Ghim Wei Ho: 0000-0003-1276-0165

DOI: 10.1021/acsnano.8b00770
ACS Nano 2018, 12, 4512−4520

Notes

The authors declare no competing financial interest.

ACKNOWLEDGMENTS

This work was supported by Ministry of Education (MOE) of Singapore under R-263-000-C85-112 and R-263-000-D08-114 grants.

REFERENCES

(1) Ozbay, E. Plasmonics: Merging Photonics and Electronics at Nanoscale Dimensions. *Science* **2006**, *311*, 189−193.
(2) Homola, J. Surface Plasmon Resonance Sensors for Detection of Chemical and Biological Species. *Chem. Rev.* **2008**, *108*, 462−493.
(3) Anker, J. N.; Hall, W. P.; Lyandres, O.; Shah, N. C.; Zhao, J.; Van Duyne, R. P. Biosensing with Plasmonic Nanosensors. *Nat. Mater.* **2008**, *7*, 442−453.
(4) Yang, D.; Yang, G.; Yang, P.; Lv, R.; Gai, S.; Li, C.; He, F.; Lin, J. Assembly of Au Plasmonic Photothermal Agent and Iron Oxide Nanoparticles on Ultrathin Black Phosphorus for Targeted Photothermal and Photodynamic Cancer Therapy. *Adv. Funct. Mater.* **2017**, *27*, 1700371.
(5) Espinosa, A.; Silva, A. K. A.; Sánchez-Iglesias, A.; Grzelczak, M.; Péchoux, C.; Desboeufs, K.; Liz-Marzán, L. M.; Wilhelm, C. Cancer Cell Internalization of Gold Nanostars Impacts Their Photothermal Efficiency In Vitro and In Vivo: Toward a Plasmonic Thermal Fingerprint in Tumoral Environment. *Adv. Healthcare Mater.* **2016**, *5*, 1040−1048.
(6) Mulvaney, P. Surface Plasmon Spectroscopy of Nanosized Metal Particles. *Langmuir* **1996**, *12*, 788−800.
(7) Xu, K.; Wang, Z.; Tan, C. F.; Kang, N.; Chen, L.; Ren, L.; Thian, E. S.; Ho, G. W.; Ji, R.; Hong, M. Uniaxially Stretched Flexible Surface Plasmon Resonance Film for Versatile Surface Enhanced Raman Scattering Diagnostics. *ACS Appl. Mater. Interfaces* **2017**, *9*, 26341−26349.
(8) Linic, S.; Christopher, P.; Ingram, D. B. Plasmonic-Metal Nanostructures for Efficient Conversion of Solar to Chemical Energy. *Nat. Mater.* **2011**, *10*, 911−921.
(9) Zheng, D.; Pang, X.; Wang, M.; He, Y.; Lin, C.; Lin, Z. Unconventional Route to Hairy Plasmonic/Semiconductor Core/Shell Nanoparticles with Precisely Controlled Dimensions and Their Use in Solar Energy Conversion. *Chem. Mater.* **2015**, *27*, 5271−5278.
(10) Tseng, W.-H.; Chiu, C.-Y.; Chou, S.-W.; Chen, H.-C.; Tsai, M.-L.; Kuo, Y.-C.; Lien, D.-H.; Tsao, Y.-C.; Huang, K.-Y.; Yeh, C.-T.; He, J.-H.; Wu, C.-I.; Huang, M. H.; Chou, P.-T. Shape-Dependent Light Harvesting of 3D Gold Nanocrystals on Bulk Heterojunction Solar Cells: Plasmonic or Optical Scattering Effect? *J. Phys. Chem. C* **2015**, *119*, 7554−7564.
(11) Ray, P. C. Size and Shape Dependent Second Order Nonlinear Optical Properties of Nanomaterials and Their Application in Biological and Chemical Sensing. *Chem. Rev.* **2010**, *110*, 5332−5365.
(12) Wang, P. L.; Lin, Z. Y.; Su, X. O.; Tang, Z. Y. Application of Au Based Nanomaterials in Analytical Science. *Nano Today* **2017**, *12*, 64−97.
(13) Fang, Z.; Zhu, X. Plasmonics in Nanostructures. *Adv. Mater.* **2013**, *25*, 3840−3856.
(14) Naik, G. V.; Shalaev, V. M.; Boltasseva, A. Alternative Plasmonic Materials: Beyond Gold and Silver. *Adv. Mater.* **2013**, *25*, 3264−3294.
(15) Zhang, P.; Wang, T.; Gong, J. Mechanistic Understanding of the Plasmonic Enhancement for Solar Water Splitting. *Adv. Mater.* **2015**, *27*, 5328−5342.
(16) Wang, M.; Ye, M.; Iocozzia, J.; Lin, C.; Lin, Z. Plasmon-Mediated Solar Energy Conversion *via* Photocatalysis in Noble Metal/Semiconductor Composites. *Adv. Sci.* **2016**, *3*, 1600024.
(17) Han, C.; Quan, Q.; Chen, H. M.; Sun, Y.; Xu, Y.-J. Progressive Design of Plasmonic Metal−Semiconductor Ensemble toward Regulated Charge Flow and Improved Vis−NIR-Driven Solar-to-Chemical Conversion. *Small* **2017**, *13*, 1602947.
(18) Wang, M.; Pang, X.; Zheng, D.; He, Y.; Sun, L.; Lin, C.; Lin, Z. Nonepitaxial Growth of Uniform and Precisely Size-tunable Core/Shell Nanoparticles and their Enhanced Plasmon-driven Photocatalysis. *J. Mater. Chem. A* **2016**, *4*, 7190−7199.
(19) Tan, C. F.; Ong, W. L.; Ho, G. W. Self-Biased Hybrid Piezoelectric-Photoelectrochemical Cell with Photocatalytic Functionalities. *ACS Nano* **2015**, *9*, 7661−7670.
(20) Zhang, N.; Li, M.; Tan, C. F.; Nuo Peh, C. K.; Sum, T. C.; Ho, G. W. Plasmonic Enhanced Photoelectrochemical and Photocatalytic Performances of 1D Coaxial Ag@Ag2s Hybrids. *J. Mater. Chem. A* **2017**, *5*, 21570−21578.
(21) Kevin, M.; Fou, Y. H.; Wong, A. S. W.; Ho, G. W. A Novel Maskless Approach Towards Aligned, Density Modulated and Multi-Junction ZnO Nanowires for Enhanced Surface Area and Light Trapping Solar Cells. *Nanotechnology* **2010**, *21*, 315602.
(22) Wong, T. J.; Lim, F. J.; Gao, M.; Lee, G. H.; Ho, G. W. Photocatalytic H_2 Production of Composite One-Dimensional TiO2 Nanostructures of Different Morphological Structures and Crystal Phases with Graphene. *Catal. Sci. Technol.* **2013**, *3*, 1086−1093.
(23) Gunawidjaja, R.; Peleshanko, S.; Ko, H.; Tsukruk, V. V. Bimetallic Nanocobs: Decorating Silver Nanowires with Gold Nanoparticles. *Adv. Mater.* **2008**, *20*, 1544−1549.
(24) Lee, S. J.; Baik, J. M.; Moskovits, M. Polarization-Dependent Surface-Enhanced Raman Scattering from a Silver-Nanoparticle-Decorated Single Silver Nanowire. *Nano Lett.* **2008**, *8*, 3244−3247.
(25) Wang, X.; Wang, R.; Zhai, H.; Shen, X.; Wang, T.; Shi, L.; Yu, R.; Sun, J. Room-Temperature Surface Modification of Cu Nanowires and Their Applications in Transparent Electrodes, SERS-Based Sensors, and Organic Solar Cells. *ACS Appl. Mater. Interfaces* **2016**, *8*, 28831−28837.
(26) Kevin, M.; Lim, G. Y. R.; Ho, G. W. Facile Control of Copper Nanowire Dimensions *via* the Maillard Reaction: Using Food Chemistry for Fabricating Large-scale Transparent Flexible Conductors. *Green Chem.* **2015**, *17*, 1120−1126.
(27) Xia, X.; Wang, Y.; Ruditskiy, A.; Xia, Y. 25th Anniversary Article: Galvanic Replacement: A Simple and Versatile Route to Hollow Nanostructures with Tunable and Well-Controlled Properties. *Adv. Mater.* **2013**, *25*, 6313−6333.
(28) Tan, C. F.; Azmansah, S. A. B.; Zhu, H.; Xu, Q. H.; Ho, G. W. Spontaneous Electroless Galvanic Cell Deposition of 3D Hierarchical and Interlaced S−M−S Heterostructures. *Adv. Mater.* **2017**, *29*, 1604417.
(29) Jin, M.; He, G.; Zhang, H.; Zeng, J.; Xie, Z.; Xia, Y. Shape-Controlled Synthesis of Copper Nanocrystals in an Aqueous Solution with Glucose as a Reducing Agent and Hexadecylamine as a Capping Agent. *Angew. Chem., Int. Ed.* **2011**, *50*, 10560−10564.
(30) Jiang, Z.; Zhang, Q.; Zong, C.; Liu, B.-J.; Ren, B.; Xie, Z.; Zheng, L. Cu-Au Alloy Nanotubes with Five-Fold Twinned Structure and their Application in Surface-enhanced Raman Scattering. *J. Mater. Chem.* **2012**, *22*, 18192−18197.
(31) El Mel, A.-A.; Chettab, M.; Gautron, E.; Chauvin, A.; Humbert, B.; Mevellec, J.-Y.; Delacote, C.; Thiry, D.; Stephant, N.; Ding, J.; Du, K.; Choi, C.-H.; Tessier, P.-Y. Galvanic Replacement Reaction: A Route to Highly Ordered Bimetallic Nanotubes. *J. Phys. Chem. C* **2016**, *120*, 17652−17659.
(32) Ye, S.; Stewart, I. E.; Chen, Z.; Li, B.; Rathmell, A. R.; Wiley, B. J. How Copper Nanowires Grow and how to Control their Properties. *Acc. Chem. Res.* **2016**, *49*, 442−451.
(33) Niu, Z.; Cui, F.; Yu, Y.; Becknell, N.; Sun, Y.; Khanarian, G.; Kim, D.; Dou, L.; Dehestani, A.; Schierle-Arndt, K.; Yang, P. Ultrathin Epitaxial Cu@Au Core−Shell Nanowires for Stable Transparent Conductors. *J. Am. Chem. Soc.* **2017**, *139*, 7348−7354.
(34) Luo, M.; Zhou, M.; Rosa da Silva, R.; Tao, J.; Figueroa-Cosme, L.; Gilroy, K. D.; Peng, H.-C.; He, Z.; Xia, Y. Pentatwinned Cu Nanowires with Ultrathin Diameters below 20 nm and Their Use as Templates for the Synthesis of Au-Based Nanotubes. *ChemNanoMat* **2017**, *3*, 190−195.

DOI: 10.1021/acsnano.8b00770
ACS Nano 2018, 12, 4512−4520

(35) Wang, L.; Chen, H.; Chen, M. Facile Synthesis and Characterization of Au−Cu, Pt−Cu Nanotubes by Sacrificial Template Method. *Mater. Res. Bull.* **2014**, *53*, 185−189.
(36) Ye, S.; Marston, G.; McLaughlan, J. R.; Sigle, D. O.; Ingram, N.; Freear, S.; Baumberg, J. J.; Bushby, R. J.; Markham, A. F.; Critchley, K.; Coletta, P. L.; Evans, S. D. Engineering Gold Nanotubes with Controlled Length and Near-Infrared Absorption for Theranostic Applications. *Adv. Funct. Mater.* **2015**, *25*, 2117−2127.
(37) He, R.; Wang, Y.-C.; Wang, X.; Wang, Z.; Liu, G.; Zhou, W.; Wen, L.; Li, Q.; Wang, X.; Chen, X.; Zeng, J.; Hou, J. G. Facile Synthesis of Pentacle Gold−Copper Alloy Nanocrystals and their Plasmonic and Catalytic Properties. *Nat. Commun.* **2014**, *5*, 4327.
(38) Bazan-Diaz, L.; Mendoza-Cruz, R.; Velazquez-Salazar, J. J.; Plascencia-Villa, G.; Romeu, D.; Reyes-Gasga, J.; Herrera-Becerra, R.; Jose-Yacaman, M.; Guisbiers, G. Gold-Copper Nanostars as Photothermal Agents: Synthesis and Advanced Electron Microscopy Characterization. *Nanoscale* **2015**, *7*, 20734−20742.
(39) Lee, K.-S.; El-Sayed, M. A. Gold and Silver Nanoparticles in Sensing and Imaging: Sensitivity of Plasmon Response to Size, Shape, and Metal Composition. *J. Phys. Chem. B* **2006**, *110*, 19220−19225.
(40) Li, J.; Cushing, S. K.; Meng, F.; Senty, T. R.; Bristow, A. D.; Wu, N. Plasmon-Induced Resonance Energy Transfer for Solar Energy Conversion. *Nat. Photonics* **2015**, *9*, 601.
(41) Clavero, C. Plasmon-Induced Hot-Electron Generation at Nanoparticle/Metal-Oxide Interfaces for Photovoltaic and Photocatalytic Devices. *Nat. Photonics* **2014**, *8*, 95−103.
(42) Liu, S.; Han, C.; Tang, Z.-R.; Xu, Y.-J. Heterostructured Semiconductor Nanowire Arrays for Artificial Photosynthesis. *Mater. Horiz.* **2016**, *3*, 270−282.
(43) Hung, S.-F.; Xiao, F.-X.; Hsu, Y.-Y.; Suen, N.-T.; Yang, H.-B.; Chen, H. M.; Liu, B. Iridium Oxide-Assisted Plasmon-Induced Hot Carriers: Improvement on Kinetics and Thermodynamics of Hot Carriers. *Adv. Energy Mater.* **2016**, *6*, 1501339.
(44) Guidelli, E. J.; Baffa, O.; Clarke, D. R. Enhanced UV Emission from Silver/ZnO and Gold/ZnO Core-shell Nanoparticles: Photoluminescence, Radioluminescence, and Optically Stimulated Luminescence. *Sci. Rep.* **2015**, *5*, 14004.
(45) Jiang, T.; Qin, X.; Sun, Y.; Yu, M. UV Photocatalytic Activity of Au@ZnO Core-Shell Nanostructure with Enhanced UV Emission. *RSC Adv.* **2015**, *5*, 65595−65599.
(46) Dkhil, S. B.; Duché, D.; Gaceur, M.; Thakur, A. K.; Aboura, F. B.; Escoubas, L.; Simon, J.-J.; Guerrero, A.; Bisquert, J.; Garcia-Belmonte, G.; Bao, Q.; Fahlman, M.; Videlot-Ackermann, C.; Margeat, O.; Ackermann, J. Interplay of Optical, Morphological, and Electronic Effects of ZnO Optical Spacers in Highly Efficient Polymer Solar Cells. *Adv. Energy Mater.* **2014**, *4*, 1400805.
(47) Chiu, Y.-H.; Chang, K.-D.; Hsu, Y.-J. Plasmon-Mediated Charge Dynamics and Photoactivity Enhancement for Au-Decorated ZnO Nanocrystals. *J. Mater. Chem. A* **2018**, *6*, 4286−4296.

DOI: 10.1021/acsnano.8b00770
ACS Nano 2018, 12, 4512−4520